This document is confidential and is proprietary to the American Chemical Society and its authors. Do not copy or disclose without written permission. If you have received this item in error, notify the sender and delete all copies.

Lyotropic Polymer Liquid Crystal Coating: Enabling Lamellar Ionic-Conductive Highways for Superior C-Rate Performance in NCM523 Cathodes

Journal:	*ACS Applied Energy Materials*
Manuscript ID	ae-2025-02323d
Manuscript Type:	Article
Date Submitted by the Author:	26-Jul-2025
Complete List of Authors:	Marium, Mayeesha; Japan Synchrotron Radiation Research Institute Aoki, Kentaro; Japan Advanced Institute of Science and Technology, Materials Science Yamamoto, Katsuhiro; Nagoya Insititue of Technology, Life Science and Applied Chemistry Suwansoontorn, Athchaya; Japan Advanced Institute of Science and Technology, School of Materials Science Ikuta, Seiya; Japan Advanced Institute of Science and Technology Hara, Mitsuo; Kagawa University Faculty of Engineering, Nagano, Shusaku; Rikkyo University College of Science, Department of Chemistry Nagao, Yuki; Japan Advanced Institute of Science and Technology , School of Materials Science Nishikawa, Kei; National Institute for Materials Science, Center for Green Research on Energy and Environmental Materials Miyazaki, Tsukasa; Kyoto University, Office of Society-Academia Collaboration for Innovation Aoki, Hiroyuki; Japan Atomic Energy Agency, J-PARC Center Kobayashi, Shigeru; The University of Tokyo, Sudare, Tomohito; The University of Tokyo, Hitosugi, Taro; The University of Tokyo, Chemistry Zettsu, Nobuyuki; Shinshu University, Materials Chemistry

SCHOLARONE™
Manuscripts

Lyotropic Polymer Liquid Crystal Coating: Enabling Lamellar Ionic-Conductive Highways for Superior C-Rate Performance in NCM523 Cathodes

Mayeesha Marium[a‡], Kentaro Aoki[b‡], Katsuhiro Yamamoto[c], Athchaya Suwansoontorn[b], Seiya Ikuta[b], Mitsuo Hara[d], Shusaku Nagano[e], Yuki Nagao[b], Kei Nishikawa[f], Tsukasa Miyazaki[g], Hiroyuki Aoki[h], Shigeru Kobayashi[i], Tomohito Sudare[i], Taro Hitosugi[i], and Nobuyuki Zettsu[* a, j]

a. Department of Materials Chemistry, Shinshu University, 4-17-1 Wakasato, Nagano, 380-8553 Japan

b. School of Materials Science, Japan Advanced Institute of Science and Technology, 1-1 Asahidai, Nomi, Ishikawa, 923-1292, Japan

c. Department of Life Science and Applied Chemistry, Graduate School of Engineering, Nagoya Institute of Technology, 466-8555 Nagoya, Japan

d. Department of Molecular Design & Engineering, Graduate School of Engineering, Nagoya University, Furo-cho, Chikusa, Nagoya, Aichi 464-8603, Japan

e. Department of Chemistry, College of Science, Rikkyo University, 3-34-1 Nishi-ikebukuro, Toshima, Tokyo 171-8501, Japan

f. Rechargeable Battery Materials Group, Center for Green Research on Energy and Environmental Materials, National Institute for Materials Science 1-1 Namiki, Tsukuba, Ibaraki 305-0044, Japan

g. Office of Society-Academia Collaboration for Innovation, Kyoto University, Sakyou-ku, Kyoto 606-8501, Japan

h. Materials and Life Science Division, J-PARC Center, Japan Atomic Energy Agency, 2-4 Shirakata, Tokai, Ibaraki 319-1195, Japan

i. Department of Chemistry, The University of Tokyo, 113-0033 Tokyo, Japan

j. Institute for Aqua-regeneration, Shinshu University, 4-17-1 Wakasato, Nagano, 380-8553 Japan

‡These authors contributed equally to work.

*Corresponding Authors. zettsu@shinshu-u.ac.jp

ABSTRACT

High C-rate capability and energy-density stability are crucial for advanced lithium-ion batteries (LIBs). However, these two characteristics typically conflict in conventional systems. Herein, a lyotropic polymer liquid crystal (LPLC)-based coating was applied to the surface of $LiNi_{0.5}Co_{0.2}Mn_{0.3}O_2$ (NCM523) cathode surface to constract a highly ion-conductive artificial cathode electrolyte interface (CEI) layer, aiming to supersede traditional CEIs for LIBs. The coating material, composed of amphiphilic lithium-substituted alkyl-sulfonated polyimide (ASPI-Li) and an appropriate amount of organic liquid electrolyte, forms nanoscale fluidic layers that act as ion-conducting highways, increasing the local concentration of Li^+ near the NCM523 surface. The layered regulation of the liquid–fluid highly accelerated the ion diffusion kinetics at the electrode/electrolyte interface and showed superior C-rate capability at ambient temperatures compared to that of conventional LIB systems. The present work, using molecular design, sheds new light on the development of next-generation artificial CEI layers for various efficient and sustainable energy-storage systems.

Keyword

Lyotropic polymer liquid crystal, polymer electrolyte, lithium-ion batteries, artificial CEI

Introduction

With the growing demand for sustainable energy-storage devices with high power and energy density, research on high-performance lithium-ion batteries (LIBs) has rapidly expanded since their commercialization in the 1990s.[1] The operation of LIBs involves the sequential or simultaneous occurrence of a multitude of reactions that complicate the investigation of their mechanisms. For example, although the degradation of liquid electrolytes during battery cycling in a certain electrochemical potential window is known to afford a solid electrolyte interface (SEI) and cathode-electrolyte interface (CEI),[2] the interactions of liquid electrolytes with electrode surfaces at the atomic/molecular level remain poorly understood. Moreover, although LIBs have been widely used, the demand for higher power densities necessitates the design of more efficient LIBs that enhance Li^+ intercalation kinetics, accelerating charge and discharge reactions.

The diffusion of lithium ions within the electrode's active material and the charge-transfer (CT) kinetics at the phase boundaries are crucial factors influencing the C-rate of quick charging; hence, investigating and improving these aspects are essential.[3] For LIBs, charge transfer involves Li^+ diffusion within the electrolyte, followed by the desolvation, adsorption, and diffusion of Li^+ through the CEI and onto the active material surface, and

Li^+ insertion into the active material. Abe *et al.*[4,5] reported that intercalation kinetics are largely determined by Li^+ desolvation rather than by Li^+ diffusion through the CEI, further demonstrating that the activation energy of desolvation is positively correlated with the interaction between lithium ions and solvents. Li^+ transfer at the ceramic-based solid electrolyte/liquid electrolyte interface was also investigated. Electrochemical impedance spectroscopy (EIS) revealed that the overall reaction kinetics were determined by the activation energy of liquid electrolyte desolvation, which exceeded that of the solid electrolyte. Jow et al.[6] identified the conditions under which charge-transfer kinetics are controlled by the desolvation of Li^+ ions or their transport through the CEI. In particular, at high temperatures, charge transfer may be limited by the diffusion of Li^+ through the active material bulk or through the CEI, whereas desolvation becomes the limiting factor in the case of an amorphous electrolyte interface or a very thin CEI.

Several strategies have been employed to modify cathode materials to enhance transport kinetics and stability against capacity degradation. These include designing a core–shell structure,[7] introducing transition-metal concentration gradients[8,9], and doping the cathodes with functional materials.[10,11] The most widely used approach to modifying cathode materials for fast charging applications is surface modification with an artificial coating.[10,12–14] The structure and composition of the solid electrolyte interface formed on

the cathode's surface from the reactions of the electrolytes play a key role in determining the Li^+ diffusion behaviors. As such, these artificial coatings can act as effective tools for controlling interfacial processes for improved electrochemical properties.[15] Several other efforts have enhanced rate performance by modifying the surface environment during cycling to achieve higher capacities at high C-rates.[3,10,16–23] For example, Charles-Blin et al demonstrated that increasing the local lithium ion concentration at the $LiCoO_2$ surface, using a Li^+-conductive amorphous $Li_2B_4O_7$ coating improved discharge kinetics.[23] Similarly, the formation of an artificial CEI layer with Li-ion conductivity on a $LiNi_{0.8}Mn_{0.1}Co_{0.1}O_2$ (NCM811) cathode surface, via a nucleophilic reaction between polysulfides and vinylene carbonate (VC), protected NCM particles from electrolyte corrosion while facilitating Li-ion transport.[10] Although conductive organic polymeric coatings have been explored to improve cyclic stability and rate performances of cathode materials, most research has focused on using inorganic oxides as coating materials.[14,24] Molecularly designed functional soft materials in the artificial CEI layer can provide greater control over interface dynamics by exploiting their passive dynamic properties, an advantage that inorganic materials do not possess.

Among such materials, lyotropic liquid crystalline (LC) electrolytes have attracted significant interest as structured electrolytes, owing to their ability to self-assemble into

ordered ionic domains that support efficient Li-ion transport. These materials, typically composed of amphiphilic small molecules or polymers, offer internal nanostructures and soft-matter dynamics that are distinct from conventional liquid or solid electrolytes. While LC-based electrolytes have been applied successfully in various battery systems, their use has so far been limited to bulk ion transport media, and their potential as interfacial modifiers remains largely unexplored.

Early foundational work by Kerr *et al.* reported the spontaneous formation of lyotropic mesophases from ionic surfactant-like small molecules, even in the absence of lithium salts.[25] This study highlighted the feasibility of using lyotropic phases for ion-conductive nanostructures, although battery operation was not demonstrated. Building on this concept, Sakuda *et al.* incorporated lithium salts into lyotropic LC systems and were the first to demonstrate their electrochemical functionality in working lithium-ion batteries.[26] These studies established the viability of LC electrolytes for practical applications, particularly within the bulk electrolyte phase.

More recently, LC-based electrolytes have gained increasing attention not only in laboratory studies but also in practical device configurations for various LIB architectures. Applications have expanded to include separators with carbonate-based systems,[27, 28] aqueous quasi-solid-state systems,[29] and lithium-metal batteries.[30,31] These studies

underscore the growing relevance of LC electrolytes in improving ion conductivity and stability, though primarily in the context of bulk media. While most previous studies have focused on LC materials as bulk electrolytes, their potential as functional interfacial coatings for electrode surfaces has not yet been fully explored.

In this study, we coated the surface of $LiNi_{0.5}Co_{0.2}Mn_{0.3}O_2$ (NCM523) with an amphiphilic lithium-substituted alkyl-sulfonated polyimide (ASPI-Li), a lyotropic polymer liquid crystal (LPLC), to enhance its electrochemical performance. Previously, Ono *et al.* demonstrated that ASPI exhibits lyotropic self-organization under humid conditions, forming structurally ordered films with high proton conductivity due to the presence of flexible alkyl side chains.[32, 33] Building on this insight, we anticipated that the lyotropic nature of ASPI-Li would promote the formation of an organized interfacial structure that facilitates lithium-ion transport at the cathode-electrolyte boundary.

In fact, significant improvements in high-rate performance were observed upon coating with ASPI-Li, accompanied by a reduction in the activation energy of charge-transfer, as confirmed by electrochemical impedance spectroscopy (EIS). These results suggest that the formation of a self-assembled interfacial environment enhanced ion accessibility and interfacial kinetics. Furthermore, the ASPI-Li layer functions as a robust CEI, suppressing parasitic reactions and stabilizing the NCM523 surface during cycling. The ultrathin

ASPI-Li coating thus acts as a multifunctional interfacial layer, combining electrochemical protection with the advantages of structurally organized soft materials.

Experimental Section

Synthesis of ASPI-Li

The polymer ASPI-Li was synthesized as follows (see also Figure S1): First, the polymerization was conducted by the reaction of pyromellitic dianhydride and 3,3'-bis(sulfopropoxy)-4,4'-diaminobiphenyl with triethylamine (TEA) in *m*-cresol under an Ar atmosphere at 150 °C for 6 h.[32] The polymer was precipitated from ice-cold acetone and then collected by centrifugation to obtain ASPI-TEA with tetraethylammonium as a cation. Ion exchange from ASPI-TEA to ASPI-Li was performed by passing an aqueous solution of the obtained polymer through an ion-exchange resin provided by Organo Corporation. The degree of cation exchange was monitored from the $-CH_3$ group of the TEA peak by ^1H nuclear magnetic resonance (NMR) using an AVANCE III 400 MHz (Bruker). After the ion exchange, the solution was removed using a rotary evaporator and dried under vacuum to obtain ASPI-Li. The molecular weight was determined by gel permeation chromatography using an LC-2000Plus (JASCO Corporation). The eluent

was a 0.121 mol/L $NaNO_3$ and 0.300 mol/L water: *N*,*N*'-dimethylformamide (3:2 v/v) mixed solvent, and the molecular weight was calculated based on the standard calibration curve created using standard poly(styrene sulfonic acid) sodium salt. The internal structure of each polyimide thin film was evaluated using polarizing optical microscopy (POM). Measurements were performed using a BX51-P microscope (Olympus) and a DP28 camera (Olympus). The data were recorded using the cellSens Controller software. The synthesized polyimides were identified using Fourier-transform infrared spectroscopy with attenuated total reflectance (ATR-FTIR). The measurements were performed using a Nicolet 6700 spectrometer (Thermo Fisher Scientific), and OMNIC software (Thermo Fisher Scientific) was used for the analysis. The obtained spectra were corrected for distortion using the advanced ATR correction feature in OMNIC.

Preparation of NCM523@ASPI-Li core–shell particles

NCM523 (5E12D, Housen Co. Ltd., Japan) powders were dispersed in a solution of ASPI in aqueous tetrahydrofuran (THF) (0.5 wt% in 1:1 THF:water) and then mixed in a planetary centrifugal conditioning mixer (ARM-310, THINKY Inc.) for 12 min and 30 s. The weight ratio of ASPI-Li to NCM523 was controlled at 1:99 by weight. The mixed solution was then vacuum-filtered using a polytetrafluoroethylene (PTFE) membrane filter (ϕ= 0.10 μm). The filtrate was then dried at 80 ˚C for 24 h in a vacuum oven.

Structural and electrochemical characterization

Field-emission scanning electron microscopy (FE-SEM, JCM-5700, JEOL Ltd., Japan) was performed at an acceleration voltage of 2 kV to study the morphology of the pristine and polymer-electrolyte-coated NCM523 powders. High-magnification images were obtained using a transmission electron microscope (TEM; JEM-ARM200F, JEOL). The sample was coated with Os to prevent damage to the Ga ion beam during sample preparation. The TEM holder was airtight and the observations were conducted at room temperature. The electron acceleration voltage was set at 200 kV. Elemental and chemical analyses were performed using electron energy loss spectroscopy (EELS) and transmission electron microscopy (TEM). The chemical states of the NCM523 powder and electrode surfaces were performed by X-ray photoelectron spectroscopy (XPS; JPS-9200, JEOL Ltd., Japan) equipped with a monochromatic Mg Kα (1253.6 eV) X-ray source at acceleration tension and intensity of 10 kV and 10 mA, respectively. The organised structure of the ASPI-Li thin film before and after adding a 1:2 (v/v) mixed solvent of ethylene carbonate (EC): dimethyl carbonate (DMC), (EC-DMC), was measured using in situ grazing-incident small-angle X-ray scattering (GIXRS). GIXRS measurements were performed using a NANOPIX instrument (Rigaku Corporation, Japan) equipped with HyPix-6000HE. A Cu *K*α line (MicroMAX-007HF) was used as a

beam source, which was further focused and collimated with a confocal multilayer mirror. The sample was placed in a homemade relative humidity (RH)-controllable chamber. The RH was controlled to 5–6% by flowing dry N_2 gas using a precise humidity control generator (Micro Equipment Inc., Tokyo, Japan) at room temperature. The collimated X-ray beam was directed at the sample with an incident angle of 0.19°. The camera length was set to 140 mm, and the direct beam was blocked using a beam stopper. An ASPI-Li thin film was fabricated on a glass substrate by spin coating using an Active Spin Coater ACT-220D (Active). ASPI-Li was dissolved in a mixed solvent of deionised water: tetrahydrofuran = 1:1. The polymer concentration of the solution was optimised to obtain a film thickness of approximately 500 nm.

The ion conductivity of ASPI-Li thin films parallel to the substrate was measured using the alternating current (AC) impedance method. ASPI-Li was spin-coated to Au interdigitated electrodes (IDE), where the gap between the electrodes was 15 μm and the full length of the IDE was 21.8 cm. The impedance of the thin films was measured using a 1260 Impedance/gain-phase analyser (Solartron Analytical), an amplifier 1296 Dielectric interface (Solartron Analytical). An AC voltage of 50 mV was applied, and the impedance was measured while scanning frequencies from 1 Hz to 1 MHz. The ionic

conductivity was measured under a continuous flow of dry N_2 gas (~5% RH) before and after the addition of EC-DMC to the surface of ASPI-Li.

Neutron reflectometry (NR) measurements were performed at BL16 SOFIA (SOFIA) and BL17 (SHARAKU)[34], which are horizontal- and vertical-type time-of-flight neutron reflectometer, respectively, located in in Japan Proton Accelerator Research Complex, Material and Life Science Experimental Facility (J-PARC MLF, Ibaraki, Japan). Neutron pulses of 25 Hz were generated with a wavelength λ band of 0.2–0.88 nm. Reflectivity profiles were recorded at reflection angles of 0.3, 0.7, 1.6, and 3.5° to obtain a q-range of 0.07–3.1 nm^{-1}. Here, q is the magnitude of the scattering vector defined by $q = 4\pi\sin\theta/\lambda$, where θ is the incident angle. The NR profiles were analysed using the MOTOFIT[35], IGOR PRO software package to obtain the scattering length density (SLD) profile along the film thickness direction. The ultrathin ASPI-Li thin film was prepared on the 50.8 mmφ CaF_2 (Pier Optics Co., Ltd.) substrate by spin-coating.

The electrochemical performance of the NCM523 electrodes was investigated using R2032 coin-type half cells. The electrodes were prepared in a dry room with dew point of less than -40 °C. The electrode slurries were composed of a 94% (w/w) active material (NCM523 or ASPI-H coated or ASPI-Li coated NCM523), 3% acetylene black (Denka

Chemical Industry Ltd., Japan), and 3% polyvinylidene fluoride (Kishida Chemical Co., Ltd., Japan). N-methyl-2-pyrrolidone (Kishida Chemical Co. Ltd., Japan) was used as the solvent for slurry preparation. After mixing these materials in a conditioning mixer (AR-300, THINKY Inc., Japan), the slurry was applied onto Al foil current collectors using a baker type adjustable film applicator (PI-1210, Hosen Ltd., Japan), followed by vacuum-drying at 120 °C overnight. After they were dried, the cathodes were cut into 14 mm circular shapes with a hand punch and pressed at 50 kN using a hydraulic press (P-1B, RIKEN KIKI Ltd., Japan). A solution of 1M $LiPF_6$ in ethylene carbonate: dimethyl carbonate (EC:DMC 1:2 v/v) was used with polypropylene (Celgard #2400) as separators. A potentio-galvanostat (VSP-300, Biologic, France) was used to measure the EIS of the half cells with 50% and 100% state of charge (SOC) within the frequency range of 200 kHz to 1.00 mHz with temperature variation. Constant current charge-discharge tests were performed with a potentiostat (HJ-SD8 series, Hokuto Denko Ltd., Japan) at a current density of 0.2–10C within the cutoff voltage range of 2.8–4.3 V. Galvanostatic intermittent titration technique (GITT) was performed with a batter testing system (Neware BTS-4008) to evaluate the Li diffusion coefficient in both bare and polymer coated NCM523 containing half-cells. The test was carried out at a constant current pulse of 0.05C for 10 min, followed by a rest for 30-min, within the voltage range of 3.5–

4.2V. Prior to all electrochemical experiments, the coin cells were cycled at a constant current (CC mode) at 0.2C rate for three cycles to induce the formation of CEIs.

Single particle galvanostatic tests

A Pt microwire 10 μm in diameter was sealed in a glass capillary.[36] The tip of the glass-sealed Pt microwire was cut to yield a microdisk and then polished carefully to a mirror face. The single-particle measurement system was operated in a super dry room. The microelectrode was manipulated using a micromanipulator (QP-2RH, MicroSupport) to contact the probe with the single-stranded NCM523@ASPI-Li core–shell particle under an optical microscope (BX-51, Olympus). The electrolyte was composed of EC and propylene carbonate (PC) (1:1, v/v) containing 1 M $LiPF_6$ (Kishida Chemical Co., Ltd.). The counter electrode was a Li foil supplied by Honjo Metal Co., Ltd., and electrochemical measurements were performed using a two-electrode system. The galvanostatic charging and discharging tests were carried out with an electrochemical analyser (SP-200, BioLogic) in the range 3.0–4.2 V vs. Li/Li^+. The ambient room temperature was maintained at 295 K.

$LiCoO_2$ thin film deposition

(001)-oriented $LiCoO_2$ epitaxial thin film of thickness 60 nm were deposited on (0001)-oriented Al_2O_3 single crystal substrate (15 × 15 × 0.5t mm, SHINKOSHA CO., Ltd.).[37] A Li-rich target, $Li_{1.2}CoO_2$, was used to compensate for the loss of Li during deposition. A KrF excimer laser (wavelength of 248 nm) was used to irradiate the target at a repetition rate of 5 Hz. The target fluence was 1.0 J/cm^2. During the deposition process, the partial pressure of oxygen was 1×10^{-6} Torr, and the substrate was kept at room temperature.

Results and Discussion

ATR-FTIR Characterisation of ASPI-Li films

Figure 1(a) shows the molecular structure of ASPI-Li. ASPI-Li was prepared using an ion-exchange reaction between a tetraethylammonium cation and a Li cation. ^{1}H NMR spectrum of ASPI-Li (Figure S2) suggests a 98.8% ion exchange rate from TEA to Li^+ ions. Furthermore, the absence of -COO^- or -NH vibration modes in the ATR-FTIR spectra of both ASPI-TEA and ASPI-Li suggested that the ring-opening of polyimide moieties was negligibly small (Figure S3). The weight-averaged molecular weight and polymer dispersity of ASPI-Li were 2.1×10^5 and 3.5, respectively.

<Figure 1>

Characterisation of organised structures in ASPI-Li thin film

The nature of the lyotropic liquid crystals was investigated by conducting POM observations on the ASPI-Li thin films (Figure 1(b)). A clear birefringence pattern was observed with a domain size of *ca*. 50 μm, indicative of the liquid crystalline nature. Furthermore, the structure of ASPI-Li under the operating conditions of a Li-ion battery was examined using GIXRS. Figures 1(c) and (d) show the changes in two-dimensional GIXRS images of 500 nm thick ASPI-2-Li thin films after adding EC-DMC. Addition of the EC-DMC solution provided a scattering signature in the out-of-plane direction near the specular region. The corresponding one-dimensional out-of-plane profiles are shown in Figure 1(e). The scattering peaks at q_1 = 1.19 nm^{-1} (5.29 nm) and its higher order scatterings ($2q_1$ and $4q_1$) can be assigned to the self-organised structure of ASPI-Li. In contrast, the scattering signals assigned to the polymer unit length disappeared completely (Figure 1(f)). ATR-FTIR spectroscopy was also performed (Figure S4). The presence of the C=O vibration mode of EC-DMC centred at 1780 cm^{-1} suggests the incorporation of EC-DMC molecules into the ASPI-Li structure. The 3.1±0.2 molecules per -SO_3Li

functional group were incorporated into ASPI-Li structures, as quantified by the weight change of the ASPI-Li thin film after the EC-DMC addition.

The scattering peaks observed in the GIXRS could be attributed to the layered periodic structure formed in the ASPI-Li thin film by the incorporation of EC-DMC molecules because the formation of the periodic structure was observed only in the out-of-plane direction. Thus, the scattering can be reasonably attributed to the lamellar structure stabilised by the phase separation of the lithium alkyl sulfonate layer of the side chain and the polyimide layer of the main chain. The scattering of ASPI-Li upon EC-DMC addition was also observed on (001)-oriented $LiCoO_2$ thin film prepared by RF magnetron sputtering (Figure S5). $LiCoO_2$ is an analogous transition metal layered compound to NCM523. This strongly supports the possibility that ASPI-Li ultrathin films deposited on the surface of NCM523 particles form similarly organised nanostructures with the assistance of lyotropic liquid crystals.

The Li-ion conductivity of the lamellar-structured ASPI-Li thin films was evaluated using AC impedance spectroscopy. Figure 1(g) shows typical Nyquist plots of the dried state and EC-DMC-incorporated ASPI-Li thin films. Although no lithium salt, such as $LiPF_6$, was added, the incorporation of EC-DMC molecules enhanced the Li-ion conductivity of

1.2×10^{-12} S·cm^{-1} to 1.3×10^{-8} S·cm^{-1}. The lithium ions of the alkyl sulfonate side chains contribute to Li-ion diffusion in the lamellar layer. Furthermore, the ion conductivity of the ASPI-Li thin film in 1 M $LiPF_6$/EC-DMC solution was comparable to that in EC-DMC without Li salt (Figure S6). This suggested that $LiPF_6$ was not incorporated into the organized structure of ASPI-Li.

<Figure 2>

Structural characterisation of NCM523@ASPI-Li

The morphological changes in the NCM523 particles after ASPI-Li thin-film coating were investigated by FE-SEM (Figures 2(a) and (b)) at different magnifications. The morphology of pristine NCM523 was preserved after coating. However, the lack of a noticeable difference between the images of the coated and uncoated materials results from the formation of an ultrathin homogeneous polymer layer with no cracks or agglomerates which is undetectable at the resolution of the FE-SEM instrument used for this study. Scanning transmission electron microscope (STEM) combined with electron energy loss spectroscopy (EELS) was used to further investigate the polymer coating layer. The defocus

technique was utilized for the STEM-EELS line analysis for preventing electron beam damage. Figures 2(c) show the line analysis and corresponding heat-map images to visualize peak position and intensity) for C in EELS (~285 eV) with a pitch of 1 nm in the upper 50 nm region from the polar surface to the inner core. The spectra attributed to the NCM523 phase and the protective Os layer were not clearly observed, however signals from the C-containing material were clearly detected. This suggests that an ASPI-Li polymer layer is formed on the surface of NCM523 particles. It is considered that the thin layer with different contrast on the NCM523 surface observed in the STEM image corresponds to the ASPI-Li layer, and the thickness of the overlayer is estimated to be 30 nm. Figure 2(d) shows a TEM image indicating the presence of an inhomogeneous coating thickness of 17–60 nm with an increase in the polymer content of the particles from 0.25% to 1%. The XPS core-level spectra of the pristine and ASPI-Li-modified powders (Table S1) also suggest the formation of a coating layer on the surface-modified NCM523 in the presence of a small percentage of sulphur and increased Li content, which is expected to originate from the structure of the ASPI-Li polymers. To gain insight into the formation of the organized structure in ultrathin ASPI-Li induced by EC-DMC, neutron reflectometry (NR) was conducted on both pristine and EC-DMC-

treated samples (Figure S7). After adding EC-DMC and drying the 15 nm ASPI-Li film, a scattering peak at 1.12 nm^{-1} was observed, close to that in the 500 nm-thick ASPI-Li film (Figure 2e). The reflectivity profiles were fitted using a two-layer model for the pristine ASPI-Li, whereas the EC-DMC-treated ASPI-Li required a model incorporating three periodic stackings of polymer and EC-DMC layers. Parameters used for NR profile analysis are summarized in Figure S7. An expansion in the total film thickness was observed upon EC-DMC treatment, and the amount of EC-DMC incorporated was estimated from the SLD to be approximately one EC-DMC molecule per SO_3Li group. These results indicate the formation of an organized structure in ultrathin ASPI-Li films, supporting the potential of ASPI-Li as a CEI material in Li-ion batteries.

<Figure 3>

Electrochemical characterisation of NCM523@ASPI-Li

Figure 3(a) shows the typical galvanostatic charge–discharge profiles of the half-cells containg a solution of 1M $LiPF_6$ in EC:DMC 1:2 v/v as an electrolyte. Evidently, the presence of the coating slightly increased discharge capacity (172 $mAh \cdot g^{-1}$) compared to

NCM523 (166 $mAh \cdot g^{-1}$) at a relatively slow discharge rate of 0.2 C. This contribution is considered to arise from the increased Li-ion conductivity of the ASPI-Li film itself, which occurs throught the incorporation of EC-DMC molecule in the organized lamellar structure.

The increse of the specific capacity by the presence of the ASPI-Li layer is obviously enhanced under the higher discharge rate conditions. Figure 3(b) shows the discharge curves at various rates ranging from 0.5C to 10C, with all charge processes performed under controlled conditions in the constant current constant voltage (cccv) mode at a constant C-rate. Compared to that observed at 0.5C, the working voltage for the solid-solution redox reaction assigned to $Co^{4+} \rightarrow Co^{3+}$ and $Ni^{4+} \rightarrow Ni^{3+}$ decreased at higher discharge C-rates in all cells, which was ascribed to the growth of internal resistance with increasing current density. The voltage drop was attenuated in comparison with that of the bare NCM523 electrode, which confirms that the ASPI-Li layer mitigated the growth of the internal resistance with increasing current density. Variations in the discharge capacities and capacity retention percentages with the number of cycles are summarised in Figure 3(c). The NCM523 and NCM523@ASPI-Li cathodes underwent significant capacity degradation with increasing C-rates. The specific capacity and working voltage also decreased significantly with increasing C-rates. This suggests that the growth of the

internal resistance, due to the Li^+ diffusion limit to the electrode surface from the bulk electrolyte with increasing current density, became tangible at a rate >4C. Notably, the effect of the ASPI-Li coating was recognisable in discharge rates between 3C to 8C. The effect of the ASPI-Li coating on capacity retention was most pronounced at a discharge rate of 4C, with the NCM523@ASPI-Li electrode showing a capacity retention gap of ~30% compared to the NCM523 electrode. This indicates that the ASPI-Li coating clearly contributes to the improved C-rate capability in the discharge process and can sufficiently mitigate capacity degradation at rates of up to 8C. Li-ion conductive ASPI-Li layer functions as an artificial CEI layer is expected to provide accelerated Li ion diffusion in the ion conductive channel by the incorporation of EC-DMC molecules. Furthermore, additional movable lithium ions of the alkyl sulfonate side chains in the lamellar layer will also contribute to Li-ion diffusion at the interface which results in the enhancement of C rate capability. The impact of the ASPI-Li coating completely vanished when the test was performed at >9C, suggesting that the effect of the ASPI-Li layer reached its limit under these conditions and that the rate-determining step shifted from Li^+ exchange or desolvation at the electrode interface to Li^+ mass transfer in the electrolyte.

Cao et al. designed a surface-modified NCM811 with a conductive polyaniline-polyethylene glycol (PANI-PEG) coating which could achieve improved rate

performance owing to the high electrical conductivity of PANI and the capability of PEG chains to form accessible diffusion pathways for Li ions.[38] In the case of NCM523@ ASPI-Li systems, the ordered liquid crystalline nature of the polymer electrolyte creates liquid–fluidic ionic channels on the electrode surface that facilitate Li diffusion, which in turn increases the local Li-ion concentration in the vicinity of the cathode surface.

The intrinsic discharge characteristics of NCM523@ASPI-Li were evaluated by performing a discharge rate performance test using a single-particle measurement technique, in which a lab-made Pt microprobe was used to make an electrical connection with one active material particle.[36] Using this technique, we can ascertain the inherent electrochemical properties of the cathode materials. This does not account for the influence of the components and properties of the electrode slurry, for example, the effect of interaction with conductive carbon, binding polymers, and the effect of cathode thickness and density. Figure 3(d) shows the galvanostatic charge–discharge profiles with a charging current of 2 nA and a discharging current of 50 nA. This demonstrates that ASPI-Li coating decreases overvoltage for the discharging reaction by 0.2 V (vs. Li/Li^+). The improvement in the interface kinetics offer a better rate performance for a single particle (Figure 3(e)). This is in agreement with the C-rate performance tests conducted for half cells with bare and ASPI-Li-coated composite electrode systems. These results

imply that the ASPI-Li coating can intrinsically enhance the electrochemical performance of the active materials, irrespective of the chemical and physical structures of the electrode composites.

<Figure 4>

Figure 4(a) shows the Nyquist plot obtained from the EIS measurements of the NCM523 and NCM523@ASPI-Li cathodes based on half cells, to gain further insight into the effect of the ASPI-Li coating on the internal resistances. Prior to EIS measurements, the coin cells were subjected to aging (cycling at 0.2C for three cycles) followed by cycling at gradually increasing C-rates from 0.5C to 5C as shown earlier in the rate performance test (Figure 3(c)), followed by charging to 50% SOC. The semicircles obtained from the Nyquist plots were fitted to the equivalent circuit model in EC-Lab software (Figure 4(b)), using the corresponding Bode plots (Figure 4(c) and 4(d)). The semicircle in the Nyquist plot comprises an overlap of two separate semicircles corresponding to the resistive components R_{CEI} and R_{CT} originating from the resistance at the CEI layer and the charge-transfer resistances, respectively. The values of these resistive elements, calculated from the equivalent circuit models, are shown in Figure 4(b). The ASPI-Li coating

reduced the total resistance and those of both the resistive elements. The significant reduction of CEI resistance can be attributed to either ASPI-Li layer with higher Li-ion conductivity as an artificial CEI formation enable Li-ion transfer with less resistance. Electronegative oxygen in the artificial CEI layer made of ASPI-Li thin film can attract Li ions from the electrolyte, thereby facilitating Li-ion conduction, which ultimately results in lower resistance at the CEI.

The lower R_{CT} for the ASPI-Li-coated systems also suggests that there is an effective interaction between the Li ions and the CEI layer. Charles-Blin et al. previously showed a similar reduction of R_{CT} in $Li_2B_4O_7$ coated $LiCoO_2$ electrodes, which was correlated with lower activation energy for Li-ion diffusion and an increase in the local concentration of Li-ions obtained from the analysis of capacitive components in EIS.[23] Similarly, in the NCM523@ASPI-Li system, a reduced R_{CT} originated from easily accessible Li-ion diffusion pathways provided by the ordered ionic channel in the ASPI-Li layer. It is considered that the ASPI-Li layer offers lowered activation energy for the desolvation of Li-ion coordinated with the alkyl sulfonate side chains in the lamellar layer and provides the enhanced local Li-ion concentration, as opposed to that of the carbonates based liquid electrolyte.

To gain a deeper understanding of the internal resistances at the electrode surfaces, we measured the activation energies of the resistance components by performing EIS measurements from 40 °C to 0 °C in 10 °C intervals at a controlled SOC of 50%. The resistances at each temperature, extracted from the equivalent circuit model, were fitted to the Arrhenius equation, and the activation energies of the individual components were calculated following the method reported by Nakayama et al.[39] Figures 4(e) and 4(f) show the temperature-dependent impedance spectra, and Figure 4(g) presents the corresponding Arrhenius plots. The resistance values at each temperature are summarized in the table in Figure 4(h).

In the Arrhenius plots, the resistance components generally exhibited linear temperature dependence, indicating thermally activated behavior. One data point deviated slightly from the linear trend, which we attribute to possible experimental error or localized variations in interfacial properties at that specific temperature. Nevertheless, the activation energies were determined from the predominant linear region, and this minor deviation does not affect the overall conclusions of the analysis.

The cathode-electrolyte interface resistance R_{CEI} was slightly more sensitive to temperature variations than R_{CT} for both bare NCM523 and NCM523@ASPI-Li. The activation energy of R_{CEI} was significantly lower for NCM523@ASPI-Li compared to

bare NCM523, while the activation energy of R_{CT} was slightly reduced by the ASPI-Li coating. The increase in impedance below 20 °C can be explained by the freezing of the segmental motion of the polymer chains in the solid electrolyte coating, which inhibits Li-ion conduction. However, the R_{CT} of the coated materials remained lower than that of the uncoated materials across the entire temperature range.

The activation energy reported for Li-ion solvation by open-chain carbonates is typically ~0.70 eV.[40-42] This suggests that the ASPI-Li coating slightly lowers the activation energy, thereby accelerating the desolvation reaction within the electric double layer formed at the electrode interface. Although the exact mechanism of ion transport enhancement in the NCM523@ASPI-Li system remains unclear, one possible explanation is that charge transfer is still facilitated despite the frozen segmental motion. This may arise from the decoupling of ion diffusion from the structural relaxation of the polymer segments, a phenomenon commonly observed in superionic systems.[43-45] These results suggest that the activation energy for lithium-ion desolvation in the lamellar layer becomes lower than that in the bulk electrolyte.

GITT was used to obtain information on the effect of the ASPI-Li coating on the diffusion of Li ions. The following equation was used to calculate the Li diffusion co-efficient during discharging.[46]

$$D_{Li^+} = \frac{4}{\pi\tau}\left(\frac{mV_M}{MA}\right)^2\left(\frac{\Delta E_S}{\Delta E_\tau}\right)^2$$

Here, V_M is the molar volume, M is the molar mass, m is the mass of the active material, and A is the electrode surface area. Figure S7 shows the diffusion coefficients for the discharge process as a function of voltage calculated from the GITT discharge curves. Li diffusion coefficients for NCM523 and NCM523@ASPI-Li coated half cells rise from 10^{-11} cm^2 s^{-1} to 10^{-8} cm^2 s^{-1}, before plateauing around 3.7 V without significant changes. Although the C-rate test implied enhanced Li-ion transport kinetics due to the ASPI-Li coating, the GITT measurements could not detect any noticeable changes. This suggests the presence of a third layer between NCM523 and the ASPI-Li interface. The authors believe that this may be an EC-DMC with a $LiPF_6$ electrolyte (slower desolvation step) or an ASPI layer with a disordered layered lamellar structure formation at the extreme surface of NCM523 (degrading Li-ion diffusion kinetics, as compared to that in the ordered lamellar structure). This was supported by the relatively broad and weak scattering in the OP scattering in LCO (Figure S5) compared with that in glass substrate (Figure 1(e).

<Figures 5>

XPS was conducted to understand the chemical states of the extrema surfaces of the NCM523@ASPI-Li electrode. Figures 5(a) and 5(b) show the XPS O1s core-level spectra of the NCM523 and NCM523@ASPI-Li cathodes surface, respectively, after aging for three cycles. The O1s spectra could be deconvoluted into four bands based on several components of the cathode materials, ASPI-Li, and the CEI layer from the reaction with the EC-DMC/$LiPF_6$ electrolyte. The spectra included spectra centred at 529.3 eV (transition metal oxide M-O bond), at 530.9 eV (Li_2CO_3 and LiOH), at 532.6 eV (C-O and C=O from organic decomposition products like $RCH_2OCOOLi$ and ASPI-Li), and 534.0 eV (attributed to $Li_xPO_yF_z$).[47-49] Compared with that in the O1s spectra of NCM523 and ASPI-Li coated NCM523, the band arising from inorganic decomposition products Li_2CO_3 and LiOH becomes smaller in the coated cathodes. The reduction of Li_2CO_3 and LiOH which are known to have insulating properties causing capacity degradation, can be assumed to contribute to the improved electrochemical performance of the polymer electrolyte-coated cathode.[11] Moreover, the components corresponding to C-O and C=O also increase noticeably in the ASPI-Li coated system which may arise from the structure of the polymer itself. These oxygen sites can be assumed to bond with Li ions in the electrolyte, resulting in improved diffusion kinetics. Figures 5(c) and 5(d) display the

Li1s and F1s spectra, showing the presence of LiF (56.2 eV in Li1s, 684.8 eV in F1s spectra) along with $LiPF_6$ and $Li_xPO_yF_z$ (687.4 eV and 685.4 eV, respectively). For bare NCM523, the spectra attributed to Li1s were not detected. The abundance of Li on the surface of the NCM523@ASPI-Li cathode suggests that the ASPI-Li layer stores Li ions in the nanochannel (sufficient for detection by XPS). The Li-rich artificial CEI layer exhibited increased ion conductivity and kinetics for the charge-transfer reaction at the interface.

Conclusion

Electrochemical analysis using coin-type half cells was performed to demonstrate the effects of ASPI-Li coating on NCM523 particles, as a functional artificial CEI layer, on the properties of the corresponding electrodes, particularly from the perspective of kinetics. The amphiphilic ASPI unit exhibited a lyotropic liquid crystal nature through a reserved 1M $LiPF_6$ salt containing the EC-DMC electrolyte, offering liquid–fluid lamellar ionic-conductive highways to the NCM523 cathode-based lithium-ion battery system. EIS analysis of the NCM523@ASPI-Li electrodes at designated SOCs revealed that the ASPI-Li layer accelerated charge transfer, which is typically limited by the desolvation

of Li ions by open-chain carbonates at the electrolyte interface. Furthermore, the calculated activation energies strongly suggested that Li^+ transfer within the ASPI-Li required less energy than the desolvation mechanism that would occur on the bare NCM523 cathode. Although the diffusion-controlled step accompanied by desolvation is widely accepted as the rate-determining process in battery reactions, our results suggest that the ASPI-Li lyotropic liquid-crystal electrolyte coating increases the local Li+ concentration and ion diffusion kinetics on the NCM523 particle surface. This shifts the rate-determining step to the reaction-controlled process. Our report is the first to provide a complete picture of the effects of coating the surface of cathode active material particles with a highly organised polymeric electrolyte composed of nanostructured ionic channels. These promising results reveal new possibilities for exploiting lyotropic liquid crystalline conductive polymers with diverse structures as artificial CEI layer materials, with the aim of enhancing the electrochemical performance in terms of kinetics.

AUTHOR INFORMATION

Corresponding Author

*E-mail: zettsu@shinshu-u.ac.jp

Author Contributions

N. Z. conceived the study. M. M., K. A, A. S, S. I, and Y. N. designed and performed the synthesis and structural characterization of ASPI-Li (K. A., A. S., S. I., and Y. N.), the preparation and electrochemical characterization experiments of NCM523@ASPI-Li (M. M., and M. N.), GI-SAXS (K. A., M. H., and S. N.), NR (K. A., K. Y., Y. N., T. M., H. A.) and single particle measurement (K. N.) and $LiCoO_2$ thin film deposition (S. K., T. S., and T. H.). N. Z., M. M., K. A., and Y. N. wrote the manuscript.

ACKNOWLEDGMENT

The authors would like to acknowledge Mr. Munenori Uno, Machine Shop in Center for Nano Materials and Technology, JAIST, for the fabrication of the humidity control chamber for GIXRS. Neutron reflectivity measurements were performed at BL16 and BL17 at the Material and Life Science Experimental Facility, J-PARC, Japan. This study was partially supported by JST-CREST (JPMJCR21B3, JPMJCR22O4), JSPS KAKENHI Grant Number 24H02203, 24K17611, and 24K01154. Neutron reflectivity measurements were performed at BL16 (2023A0162, 2024A0066) and BL17 (2018B010) at the Material and Life Science Experimental Facility, J-PARC, Japan.

REFERENCES

1 J. B. Goodenough and K.-S. Park, *J. Am. Chem. Soc*, 2013, 135, 1167–1176.

2 A. Manthiram, *Nat. Commun*, 2020, 11, 1550

3 M. Weiss, R. Ruess, J. Kasnatscheew, Y. Levartovsky, N. R. Levy, P. Minnmann, L. Stolz, T. Waldmann, M. Wohlfahrt-Mehrens, D. Aurbach, M. Winter, Y. Ein-Eli and J. Janek, *Adv Energy Mater*, 2021, 11, 2101126.

4 T. Abe, H. Fukuda, Y. Iriyama and Z. Ogumi, *J. Electrochem. Soc.*, 2004, 151, A1120.

5 T. Abe, F. Sagane, M. Ohtsuka, Y. Iriyama and Z. Ogumi, *J. Electrochem. Soc.*, 2005, **152**, A2151.

6 T. R. Jow, S. A. Delp, J. L. Allen, J.-P. Jones and M. C. Smart, *J. Electrochem. Soc.*, 2018, **165**, A361–A367.

7 S.-T. Myung, K.-S. Lee, D.-W. Kim, B. Scrosati and Y.-K. Sun, *Energy Environ*

Sci, 2011, 4, 935–939.

8 H.-J. Noh, Z. Chen, C. S. Yoon, J. Lu, K. Amine and Y.-K. Sun, *Chem. Mater.*, 2013, 25, 2109–2115.

9 X. Xu, L. Xiang, L. Wang, J. Jian, C. Du, X. He, H. Huo, X. Cheng and G. Yin, *J Mater Chem A*, 2019, 7, 7728–7735.

10 S. Wang, A. Dai, Y. Cao, H. Yang, A. Khalil, J. Lu, H. Li and X. Ai, *J Mater Chem A*, 2021, 9, 11623–11631.

11 Z. Ye, L. Qiu, W. Yang, Z. Wu, Y. Liu, G. Wang, Y. Song, B. Zhong and X. Guo, *Chemistry - A European Journal*, 2021, 27, 4249–4269.

12 Z. Chen, H. D. Nguyen, M. Zarrabeitia, H. P. Liang, D. Geiger, J. K. Kim, U. Kaiser, S. Passerini, C. Iojoiu and D. Bresser, *Adv Funct Mater*, 2021, 31, 2105343.

13 Z. Chen, Z. Wang, G.-T. Kim, G. Yang, H. Wang, X. Wang, Y. Huang, S. Passerini and Z. Shen, *ACS Appl Mater Interfaces*, 2019, 11, 26994–27003.

14 E. H. Lee, J. H. Park, J. H. Cho, S. J. Cho, D. W. Kim, H. Dan, Y. Kang and S. Y. Lee, *J Power Sources*, 2013, 244, 389–394.

15 D. Zuo, G. Tian, X. Li, D. Chen and K. Shu, *J Alloys Compd*, 2017, 706, 24–40.

16 Y. Li and Y. Qi, *Energy Environ Sci*, 2019, 12, 1286–1295.

17 J.-J. Pan, B. Chen, Y. Xie, N. Ren and T.-F. Yi, *Mater Lett*, 2019, 253, 136–139.

18 U. Nisar, R. Amin, R. Essehli, R. A. Shakoor, R. Kahraman, D. K. Kim, M. A. Khaleel and I. Belharouak, *J Power Sources*, 2018, 396, 774–781.

19 Q. Wu, X. Zhang, S. Sun, N. Wan, D. Pan, Y. Bai, H. Zhu, Y.-S. Hu and S. Dai, *Nanoscale*, 2015, 7, 15609–15617.

20 M. Wang, X. Feng, H. Xiang, Y. Feng, C. Qin, P. Yan and Y. Yu, *Small Methods*, 2019, 3, 1900355.

21 T. Teranishi, Y. Yoshikawa, R. Sakuma, H. Hashimoto, H. Hayashi, A. Kishimoto and T. Fujii, *Appl Phys Lett*, 2014, 105, 143904.

22 S. Yasuhara, S. Yasui, T. Teranishi, Y. Yoshikawa, T. Taniyama and M. Itoh, *Electrochem commun*, 2019, 109, 106604.

23 Y. Charles-Blin, K. Nemoto, N. Zettsu and K. Teshima, *J Mater Chem A*, 2020, 8, 20979–20986.

24 Z. Chen, Y. Qin, K. Amine and Y. K. Sun, *J Mater Chem*, 2010, 20, 7606–7612.

25 R. L. Kerr., S. A, Miller, R. K. Shoemaker, B. J. Elliott, D. L. Gin*, *J. Am. Chem. Soc.*, 2009, *131*, 15972-15973

26 J. Sakuda, E. Hosono, M. Yoshio, T. Ichikawa, T. Matsumoto, H. Ohno, H. Zhou, T. Kato, *Adv. Func. Mater.*, 2015, 25, 1206

27 X. Wang, X. Xu, S. Pu, Y. Huang, W. Ren, C. Luo, L. Fu, J. Xiao, W. Zeng, L. Liu,

X. Li, M. Wang, H. Cao, X. Ma, *J. Colloid Interf. Sci*., 2025, 682, 784-794.

28 X. Wang, Y. Huang, W. Ren, C. Luo, X. Xu, Y. Wang, Y. Wang, C. Zhang, Z. Zhao, L. Liu, X. Li, M. Wang, H. Cao, *Chem. Eng. J.*, 2024, 502, 158155.

29 W. Ren, Z. Hou, L. Su, X. Gao, Y. Chu, L. Zheng, F. Lu, *Chem. Eng. J.*, 2024, 501, 157794.

30 Y. Jiang, L. Liu, Y. Liu, J. Guan, H. Wang, M. Zhang, L. Chen, Y. Cao, R. Li, Y. Zhou, Q. Zeng, Z. Li, W. Liu, X. Li, L. Zhang, *Adv. Funct., Mater*., 2025, 15, 2502613.

31 X. Miao, Z. Wu, W. Hu, L. Guo, C-W. Nan, *Adv. Energy., Mater*., 2025, 15, 2500566

32 Y. Ono, R. Goto, M. Hara, S. Nagano, T. Abe and Y. Nagao, *Macromolecules*, 2018, 51, 3351–3359.

33. Y. Nagao, T. Tanaka, Y. Ono, K. Suetsugu, M. Hara, G. Wang, S. Nagano and T. Abe, *Electrochim Acta*, 2019, 300, 333–340.

34. N. L. Yamada, N. Torikai, K. Mitamura, H. Sagehashi, S. Sato, H. Seto, T. Sugita, S. Goko, M. Furusaka, T. Oda, M. Hino, T. Fujiwara, H. Takahashi, A. Takahara, *Eur. Phys. J. Plus*, 2011, 126, 108.

35. A. Nelson, *J. Appl. Cryst*., 2006. 39, 273-276

36 K. Nishikawa, N. Zettsu, K. Teshima and K. Kanamura, *Electrochemistry*, 2017, 85, 72–76.

37. S. Kobayashi, E. F. Aruguelles, T. Shirasawa, S. Kasamatsu, K. Shimizu, K. Nishio, Y. Watanabe, R. Shimizu, S. Watanabe, T. Hitosugi, *ACS Appl. Mater. Interface*, 2022, 14, 2703.

38 Y. Cao, X. Qi, K. Hu, Y. Wang, Z. Gan, Y. Li, G. Hu, Z. Peng and K. Du, *ACS Appl Mater Interfaces*, 2018, 10, 18270–18280.

39 M. Nakayama, H. Ikuta, Y. Uchimoto and M. Wakihara, *J Phys Chem B*, 2003, 107, 10603–10607.

40 J. H. Cho, G. W. Lee and Y. S. Yang, Ferroelectrics, 1997, 196, 121–124.

41 K. Xu, A. Von Cresce and U. Lee, Langmuir, 2010, 26, 11538–11543

42 V. Bocharova and A. P. Sokolov, *Macromolecules*, 2020, 53, 4141–4157.

43 Y. Wang, F. Fan, A. L. Agapov, X. Yu, K. Hong, J. Mays and A. P. Sokolov, *Solid State Ion*, 2014, 262, 782–784.

44 F. Fan, Y. Wang, T. Hong, M. F. Heres, T. Saito and A. P. Sokolov, *Macromolecules*, 2015, 48, 4461–4470.

45 D. W. Kim, N. Zettsu, H. Shiiba, G. Sánchez-Santolino, R. Ishikawa, Y. Ikuhara and K. Teshima, *J Mater Chem A*, 2020, 8, 22302–22314.

46 Y. Charles-Blin, H. Todoki, N. Zettsu and K. Teshima, *Mater Adv*, 2021, 2, 5406–5414.

47 P. Bai, X. Ji, J. Zhang, W. Zhang, S. Hou, H. Su, M. Li, T. Deng, L. Cao, S. Liu, X. He, Y. Xu and C. Wang, *Angew. Chem. Inter. Ed.,* 2022, 61, e202202731.

48 A. Wang, S. Kadam, H. Li, S. Shi and Y. Qi, *npj Comput. Mater.*, 2018, 4, 1–26.

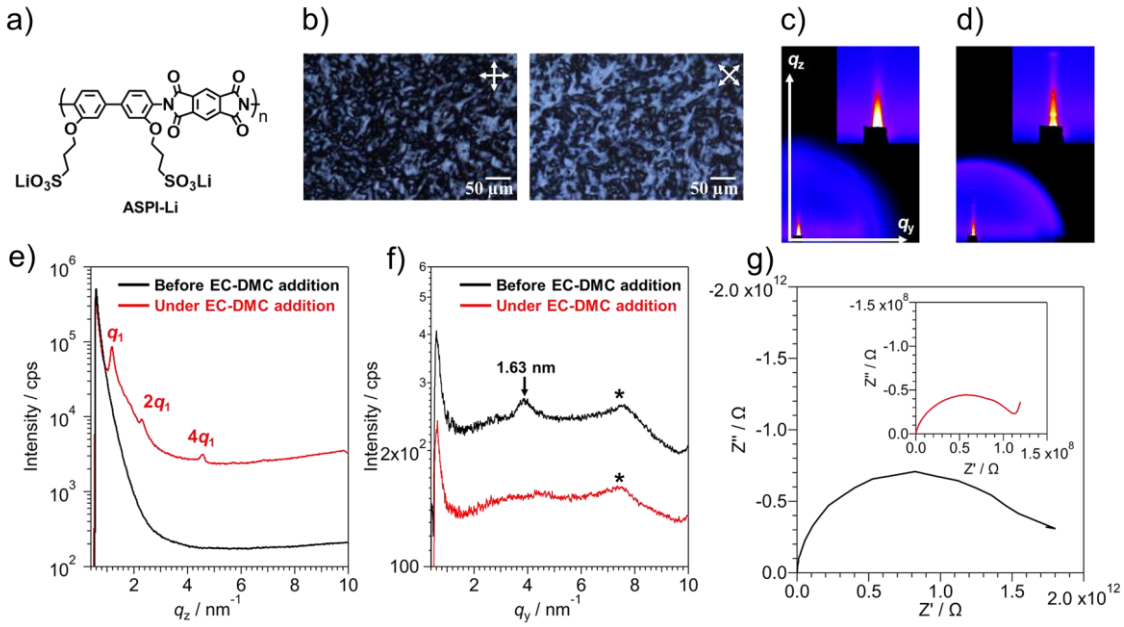


Figure 1. a) Synthetic scheme of ASPI-Li. b) Polarized optical microscope (POM) images of ASPI-Li thin films prepared on glass substrate recorded at room temperature with various cross-nicol arrangements. c) and d) Two dimensional (2D) GIXRS images of ASPI-2Li thin films c) initial and d) after adding EC-DMC solvent. Insets show the enlarged view around the specular region. e) Out-of-plane projected profiles of panels c) and d). Black and red lines denote the initial (dry state) and after EC-DMC addition, respectively. g) (black) Nyquist plots of ASPI-Li at 298 K under dry N2 gas flow condition (ca. 5% RH). Inset shows Nyquist plots of ASPI-Li taken after EC-DMC incorporation.

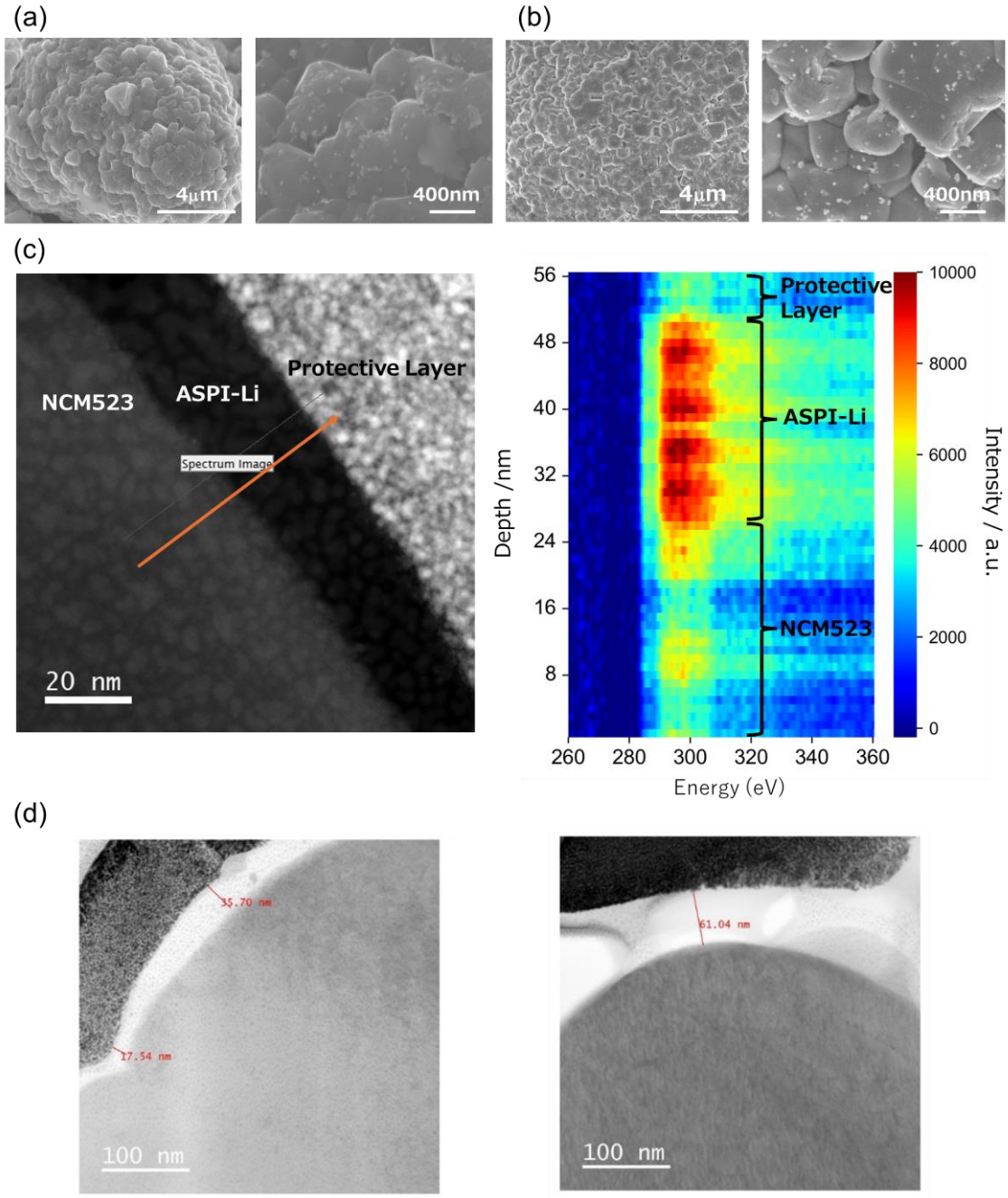


Figure 2. (a, b) FE-SEM images of (a) NCM523 (b) NCM523@ASPI-Li particles with varying magnifications, (c) Cross-sectional STEM images of NCM523@ASPI-Li particles and corresponding line analysis for C, evaluated by EELS spectroscopy by 1 nm pitch. (d)Cross-sectional TEM images of NCM523@ASPI-Li particles.

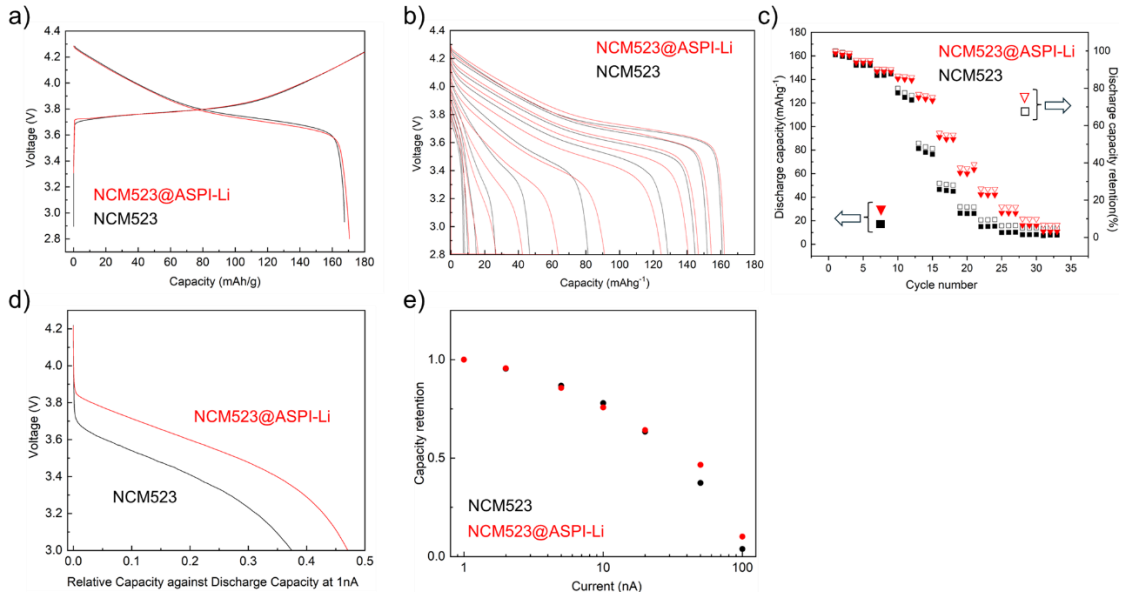


Figure 3(a) Galvanostatic charge-discharge profiles of half-cells at 0.2C for NCM523 and NCM523@ASPI-Li, (b) discharge curves and (c) discharge capacities and capacity retention, recorded at 0.2,0.5, 1, 2, 3, 4, 5, 6, 7, 8, 9 and 10 C for NCM523 and NCM523@ASPI-Li, recorded at room temperature, (d) the galvanostatic charge-discharge profiles with 2 nA charging current and 50 nA discharging current, e) variation of discharge capacity of the single particles with current in logarithmic scale: NCM523 and NCM523@ASPI-Li.

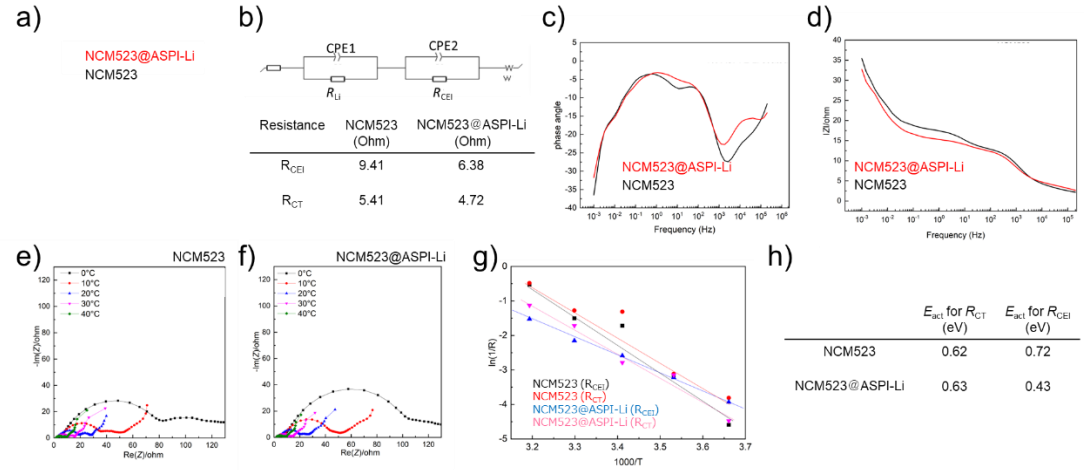


Figure 4(a) Nyquist plots obtained from EIS measurements of internal resistances of half cells with 50% SOC for NCM523 and NCM523@ASPI-Li; (b) the equivalent circuit model and corresponding values of the resistive elements calculated from this model in tabular form and corresponding Bode plots with (c) variation of phase angle with frequency and (d) variation of impedance magnitude with frequency; (e) and (f) showing Nyquist plots of NCM523 and NCM523@ASPI-Li containing half cells at temperatures of 0, 10, 20, 30 and 40°C and (g) the corresponding Arrhenius plots of ln(1/R) generated (h) calculated values of activation energies from the Arrhenius plots.

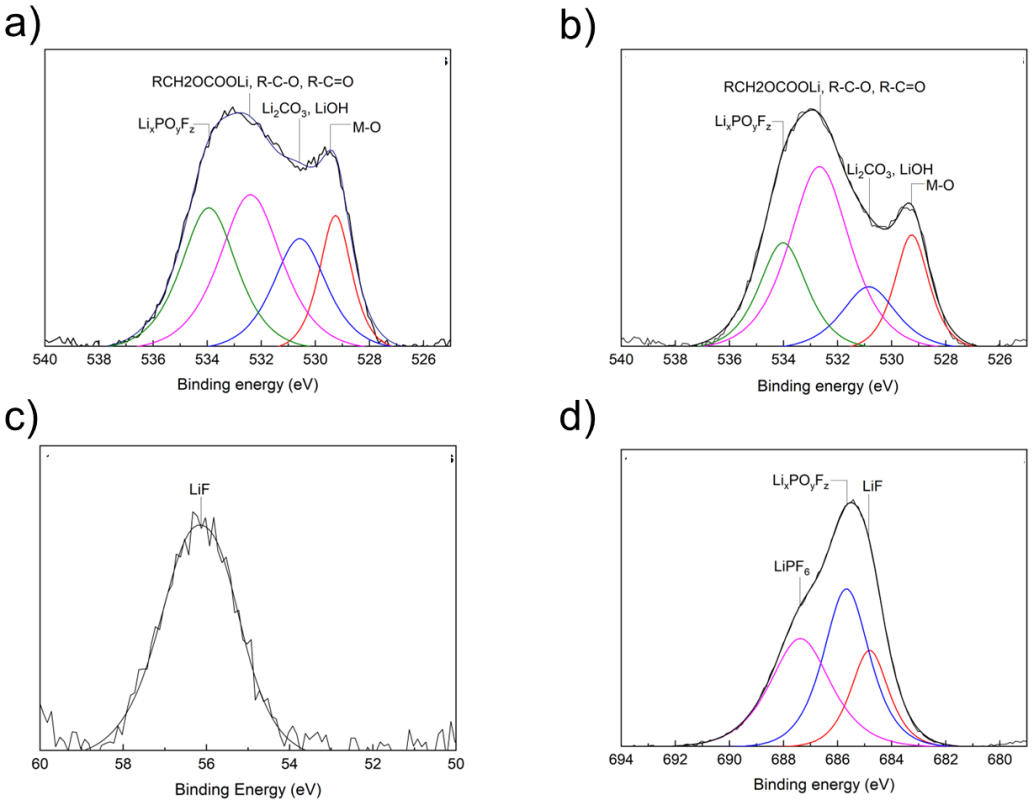


Figure 5. XPS core-level spectra of NCM523 and NCM523@ASPI-Li cathodes; (a, b) O1s spectra of (a) NCM523 (b) NCM523@ASPI-Li; (c) Li1s and (d) F1s spectra of NCM523@ASPI-Li cathode. All XPS spectroscopies were conducted to the cathodes surface taken after 1st three cycles for aging process.

Supporting information

Lyotropic Polymer Liquid Crystal Coating: Enabling Lamellar Ionic-Conductive Highways for Superior C-Rate Performance in NCM523 Cathodes

Mayeesha Marium[a‡], Kentaro Aoki[b‡], Katsuhiro Yamamoto[c], Athchaya Suwansoontorn[b], Seiya Ikuta[b], Mitsuo Hara[d], Shusaku Nagano[e], Yuki Nagao[b], Kei Nishikawa[f], Tsukasa Miyazaki[g], Hiroyuki Aoki[h], Shigeru Kobayashi[i], Tomohito Sudare[i], Taro Hitosugi[i], and Nobuyuki Zettsu[* a, j]

a. Department of Materials Chemistry, Shinshu University, 4-17-1 Wakasato, Nagano, 380-8553 Japan

b. School of Materials Science, Japan Advanced Institute of Science and Technology, 1-1 Asahidai, Nomi, Ishikawa, 923-1292, Japan

c. Department of Life Science and Applied Chemistry, Graduate School of Engineering, Nagoya Institute of Technology, 466-8555 Nagoya, Japan;

d. Department of Molecular Design & Engineering, Graduate School of Engineering, Nagoya University, Furo-cho, Chikusa, Nagoya, Aichi 464-8603, Japan

e. Department of Chemistry, College of Science, Rikkyo University, 3-34-1 Nishi-ikebukuro, Toshima, Tokyo 171-8501, Japan

f. Rechargeable Battery Materials Group, Center for Green Research on Energy and Environmental Materials, National Institute for Materials Science 1-1 Namiki, Tsukuba, Ibaraki 305-0044, Japan

g. Office of Society-Academia Collaboration for Innovation, Kyoto University, Sakyou-ku, Kyoto 606-8501, Japan

h. Materials and Life Science Division, J-PARC Center, Japan Atomic Energy Agency, 2-4 Shirakata, Tokai, Ibaraki 319-1195, Japan

i. Department of Chemistry, The University of Tokyo, 113-0033 Tokyo, Japan

j. Institute for Aqua-regeneration, Shinshu University, 4-17-1 Wakasato, Nagano, 380-8553 Japan

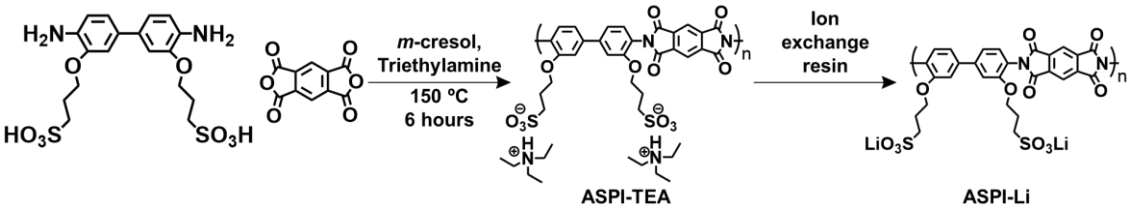


Figure S1. Synthetic scheme of ASPI-Li.

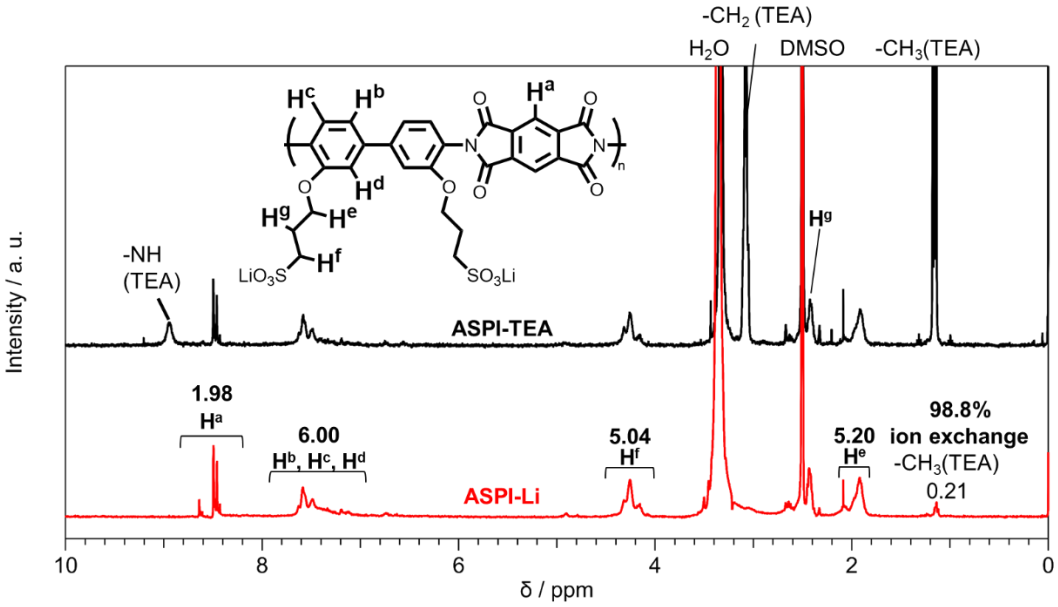


Figure S2. ^{1}H NMR spectrum of (black) ASPI-TEA and (red) ASPI-Li in DMSO-d_6.

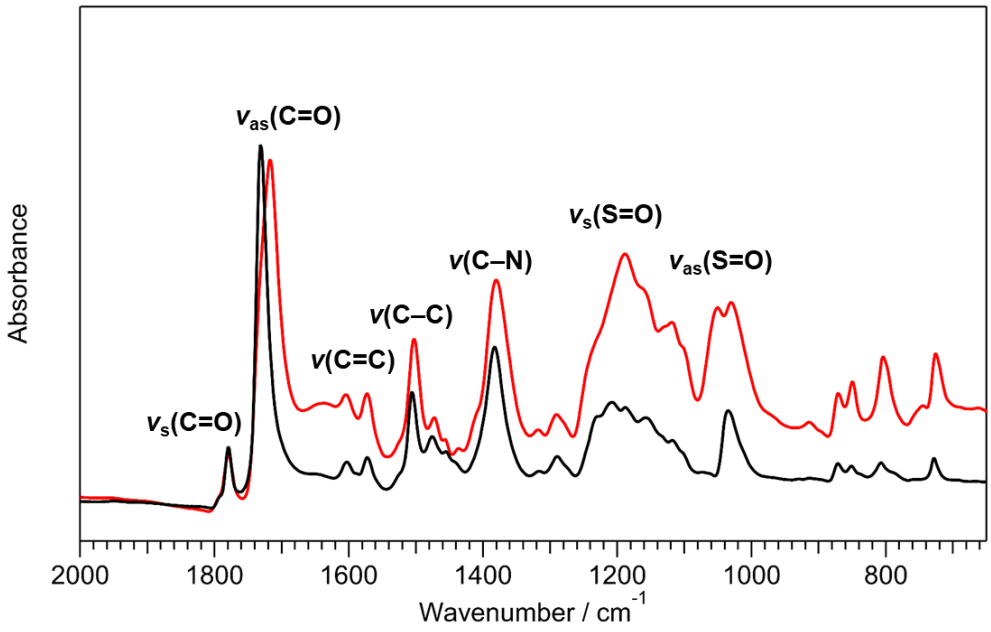


Figure S3. ATR-IR spectra of (black) ASPI-TEA and (red) ASPI-Li.

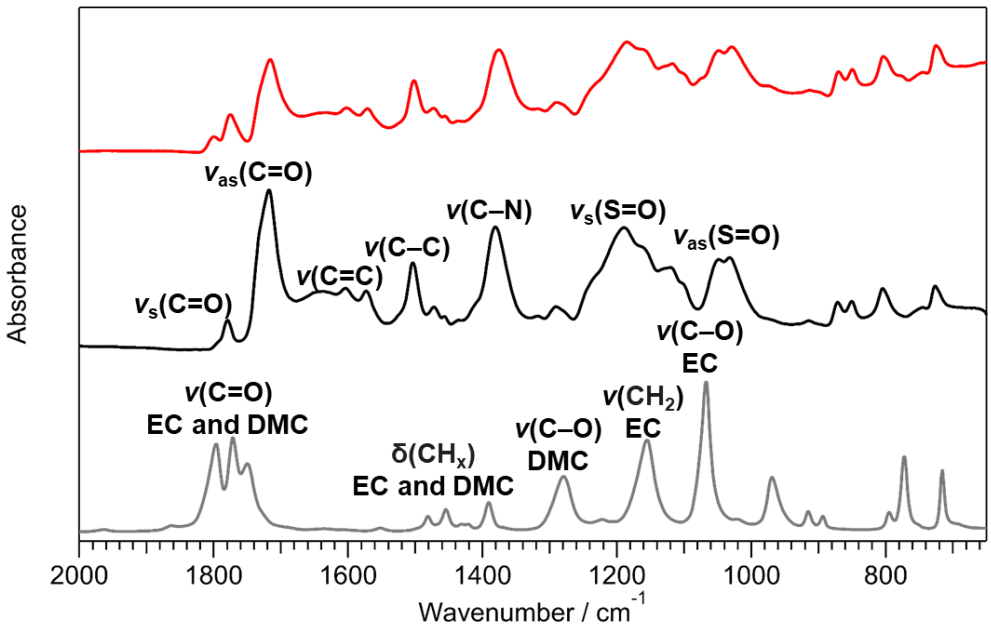


Figure S4. ATR-IR spectra of (grey) EC-DMC, (black) ASPI-Li and (red) ASPI-Li after dispersing in EC-DMC, then washed with acetone.

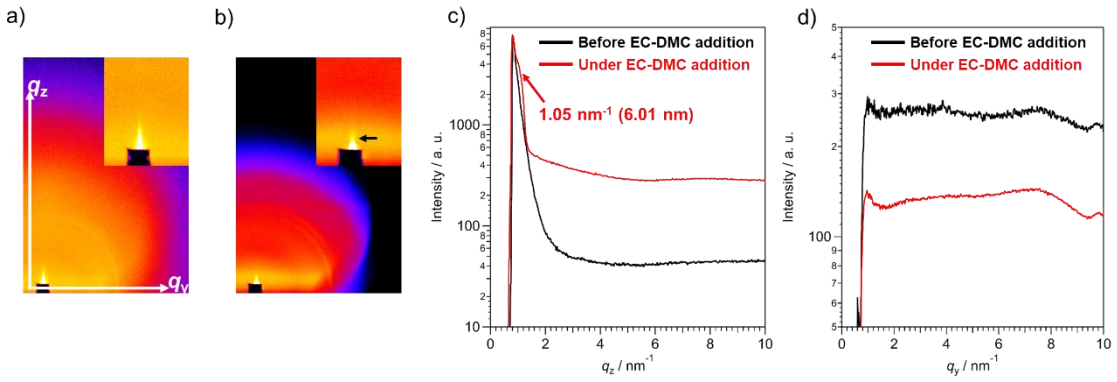


Figure S5. GIXRS results of ASPI-Li thin films on ca 60 nm thick $LiCoO_2$ layer deposited on a sapphire substrate. a) and b) 2D GIXRS images a) before and b) after EC-DMC addition. Inset shows the enlarged image around the specular region. Black arrow indicates the new scattering after EC-DMC addition. c) and d) c) Out-of-plane and d) in-plane projected profiles of panels a) and b). Black and red lines denote the before and after EC-DMC addition, respectively.

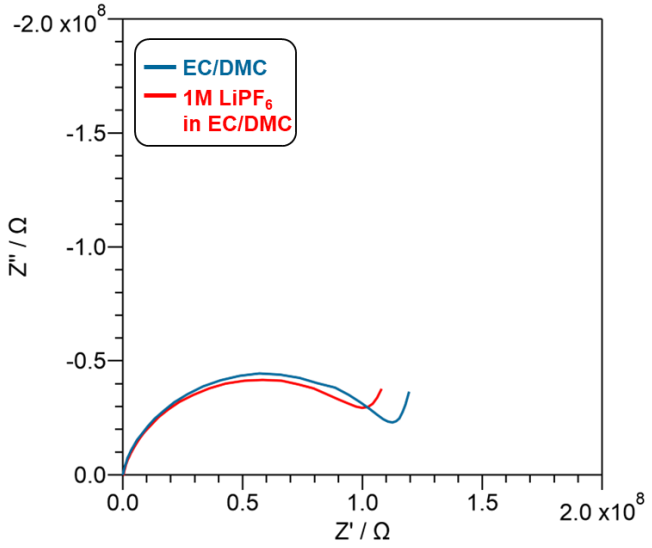
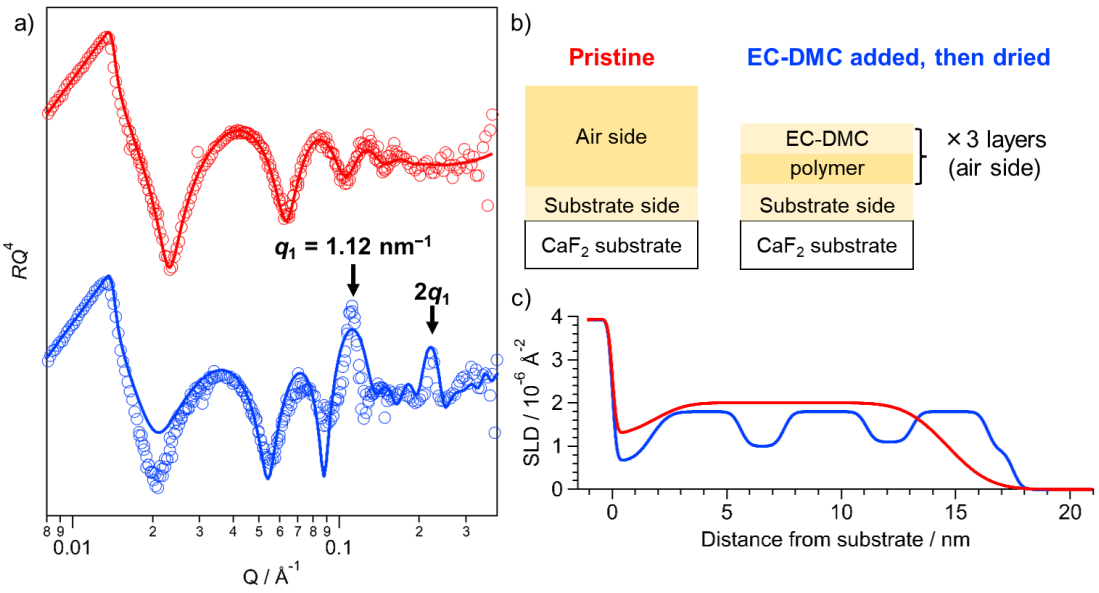


Figure S6. Nyquist plots of ASPI-Li taken at 298 K under dry N2 gas flow condition (*ca.* 5% RH). Red and blue plots were taken after EC-DMC and 1 M $LiPF_6$/EC-DMC incorporation, respectively.



d)

thickness / nm	Density
(air) 14.1±1.2	1.31
(substrate) 0.8±1.5	0.42

thickness / nm	EC-DMC /SO_3Li
(air) 15.8±1.3	0.8
(substrate) 1.7±0.6	1.1

Figure S7. a). NR profiles of of (red) pristine ASPI-Li thin films. and (blue) the same thin film once EC-DMC added, then dried on a CaF_2 substrate. Open circles and solid lines denote the experimental data and fitting lines, respectively. b) fitting models, c) SLD profiles and d) fitted parameters.

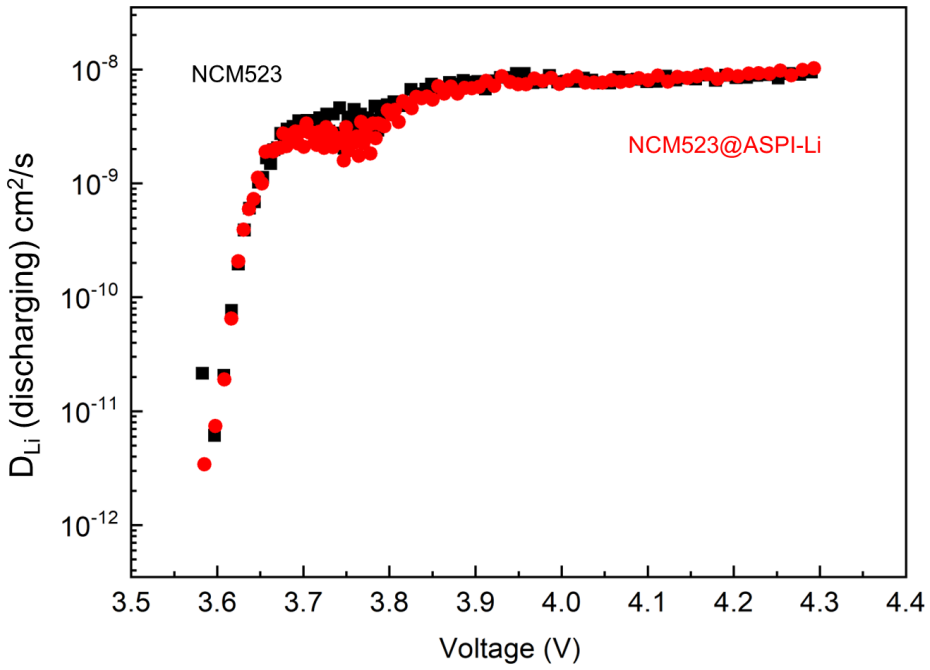


Figure S8. Diffusion coefficients for discharge process as a function of voltage calculated from GITT discharge curves: NCM523 (black), NCM523@ASPI-Li (red).

Table S1. Atomic percentages of selected elements obtained from XPS measurements of pristine NCM523 and 1% ASPI-2-Li coated NCM523

Atomic (%)	C	O	Ni	Co	Mn	Li	S
NCM523	49.3	31.5	1.5	0.77	2.1	14.8	
NCM523@ASPI-Li	42.3	28.1	1.9	1.1	2.4	23.7	0.45